

Stable time rondeau crystals in dissipative many-body systems

Zhuocheng Ma,¹ Jin Yan,² Hongzheng Zhao,^{1,*} and Liang-You Peng^{1,3,4,†}

¹*State Key Laboratory of Artificial Microstructure and Mesoscopic Physics, School of Physics, Peking University, Beijing 100871, China*

²*Weierstrass Institute for Applied Analysis and Stochastics, Mohrenstr. 39, 10117, Berlin, Germany*

³*Frontiers Science Center for Nano-Optoelectronics, Peking University, Beijing 100871, China*

⁴*Collaborative Innovation Center of Extreme Optics, Shanxi University, Taiyuan 030006, China*

(Dated: February 25, 2025)

Driven systems offer the potential to realize a wide range of non-equilibrium phenomena that are inaccessible in static systems, such as the discrete time crystals. Time rondeau crystals with a partial temporal order have been proposed as a distinctive prethermal phase of matter in systems driven by structured random protocols. Yet, heating is inevitable in closed systems and time rondeau crystals eventually melt. We introduce dissipation to counteract heating and demonstrate stable time rondeau crystals, which persist indefinitely, in a many-body interacting system. A key ingredient is synchronization in the non-interacting limit, which allows for stable time rondeau order without generating excessive heating. The presence of many-body interaction competes with synchronization and a de-synchronization phase transition occurs at a finite interaction strength. This transition is well captured via a linear stability analysis of the underlying stochastic processes.

Introduction.— Identifying different forms of order and disorder is an everlasting research subject in science. In thermal equilibrium, the spontaneous symmetry breaking leads to a long-range spatial order. In periodically driven (Floquet) systems, a discrete time crystalline (DTC) order can be similarly defined [1–3], where the discrete time translational symmetry is broken. By using quasi-periodic drives, one goes beyond this Floquet lore [4–12], establishing the deterministic, yet non-periodic, quasicrystalline temporal order [13–15].

Interestingly, the organization principle of the natural world is far richer than merely being deterministic. In fact, order and disorder can naturally coexist in our daily life: the oxygen ions in ice establish the long-range spatial order, while the location of protons bonding the oxygen ions is highly disordered. Despite the ubiquity of such partial order in space, one of its temporal cousins - the time rondeau crystal (TRC) - has not been discovered until very recently [16, 17]. Induced by structured random drives, TRCs exhibit both stroboscopic long-time order and short-time disorder at all other times, notably enriching the classification of non-equilibrium temporal orders. It is different from the conventional Floquet DTC, where the micromotion within a drive cycle exhibits the same temporal order as the stroboscopic evolution.

Yet, randomness in the driving typically opens additional heating channels [18–21], which even many-body localization can not prevent [22–25]. Indeed, TRC in a closed system appears to be a transient meta-stable (prethermal) phenomenon [26–49]: although an increasing driving frequency parametrically prolongs its lifetime, eventual heat death seems inevitable for any fixed frequency [16, 17]. One fundamental question thus arises: Are there types of TRCs that are absolutely stable to

arbitrary perturbations of both the initial state and the equations of motion (EOM), s.t. they are infinitely long-lived in the thermodynamic limit?

One potential way to avoid heating is by introducing dissipation, a strategy applicable to both quantum and classical systems [50–55]. Dissipation can generate contractive dynamics around target attractors with desired features, like the DTC order [56–60], and perturbations can be strongly damped. Yet, applying this idea to stabilize TRC requires addressing two formidable challenges: (i) Stroboscopic temporal order can be fragile when the drive involves randomness. For instance, as illustrated in Ref. [61], temporal fluctuations akin to a finite-temperature bath can lead to DTC order with a finite lifetime. (ii) The complex interplay between dissipation and many-body interactions makes it unclear how to ensure the stability of TRC in the thermodynamic limit.

We provide an affirmative answer by studying systems with multistability, i.e., multiple attractors coexist s.t. the system evolves to one of them after a sufficiently long waiting time T , a ubiquitous feature in dissipative systems [62–65]. Perhaps one of the simplest physical examples is the periodically kicked classical rotor system in the presence of damping [66], exhibiting a tunable number of fixed points in the phase space. We introduce a random protocol with a minimal “dipolar” correlation that enables precise transition rules between these fixed points. Therefore, the rotor randomly traverses multiple pathways between states and returns to the same initial state after a complete dipolar kick, cf. Fig. 1, thereby establishing the rondeau order without inducing excessive heating. Remarkably, a simple analysis of the concomitant Markovian chain reveals that synchronization occurs [67–74]: even for a randomly distributed initial ensemble of non-interacting rotors, the system inevitably exhibits synchronized motion with stable rondeau order.

The presence of many-body interactions and a finite

* hzhao@pku.edu.cn

† liangyou.peng@pku.edu.cn

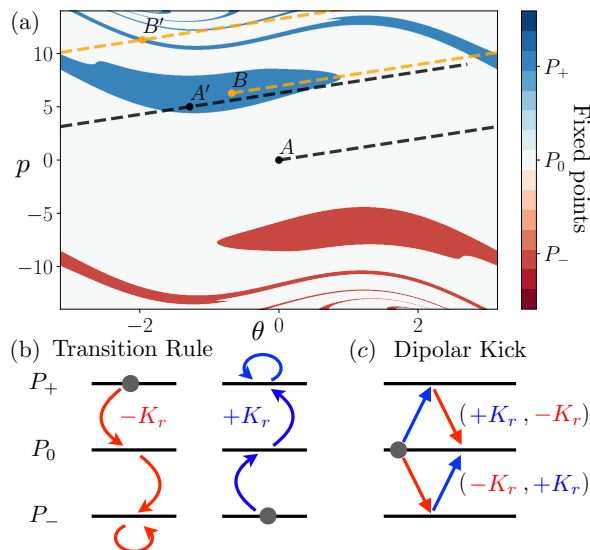


FIG. 1. (a) Basins of fixed points in the dissipative kicked rotor model. Transition rules at stroboscopic times can be determined by tuning the random kick strength K_r . For instance, after a positive kick $+K_r$, the rotor can suddenly jump from point A to A' , which is located in the basin of the fixed point P_+ (blue), realizing $P_0 \rightarrow P_+$. (b) Exact transition rules. (c) A dipolar kick induces a time rondeau order without generating unwanted heating.

waiting time T introduces uncertainties in the transition rules, which compete with perfect synchronization. Our central finding is that the synchronized phase remains robust against perturbations, with a de-synchronization phase transition occurring at a finite critical interaction strength in the thermodynamic limit. Finally, to investigate the asymptotic behavior of spatial fluctuations, we perform a linear stability analysis, which quantitatively captures the phase boundary obtained by many-body simulations.

Random kicked one-rotor model.— We start from a periodically kicked rotor described by the Hamiltonian $H(t) = p^2/2 - K_0 \cos \theta \sum_n \delta(t-n)$. By introducing damping, we obtain the discretized equations of motion

$$\begin{aligned} p(t+1) &= \gamma p(t) - K_0 \sin \theta(t), \\ \theta(t+1) &= \theta(t) + p(t+1) \pmod{2\pi}, \end{aligned} \quad (1)$$

where (p, θ) denote the angular momentum and the angle, γ is the dissipation rate, and K_0 is the strength of periodic kicks [66]. The long-time behavior of the system depends on specific parameter values, which we fix as $\gamma=0.8, K_0=2$, such that the system exhibits three stationary states, or fixed points: $(\Theta_- = \arcsin(2\pi(1-\gamma)/K_0), P_- = -2\pi)$, $(\Theta_0 = 0, P_0 = 0)$, $(\Theta_+ = -\arcsin(2\pi(1-\gamma)/K_0), P_+ = +2\pi)$.

Their corresponding basins are depicted in Fig. 1(a). After a sufficiently long waiting time T , any initial condition in a colored region will asymptotically evolve towards the corresponding fixed point.

Supposing initially the system is located at one of the fixed points, we now introduce an additional random kick with the Hamiltonian $V(t) = -\sum_m K(t)\theta\delta(t-mT)$ where $K(t)$ takes a binary value $\pm K_r$, and we dub mT (m takes integer values) as stroboscopic times. Consequently, a sudden change occurs at $t = mT$, $p \rightarrow p \pm K_r$ and $\theta \rightarrow \theta \pm K_r \pmod{2\pi}$. For simplicity, we consider $T \rightarrow \infty$ such that before the next random kick, the rotor can equilibrate again at one of the three fixed points. Therefore, $V(t)$ induces precise transitions between different fixed points without generating excessive heating.

Clearly, such a transition strongly depends on the specific value of K_r . For example, if we choose $K_r \in (4.93, 5.06)$ [75] and consider a rotor starting from the fixed point (Θ_0, P_0) , point A in Fig. 1(a). After a positive kick $+K_r$, the rotor suddenly jumps from point A to A' , which is located in the basin of the fixed point P_+ , the blue region in Fig. 1(a). Therefore, between two neighboring stroboscopic times, the transition $P_0 \rightarrow P_+$ is realized. On the other hand, if the initial point starts from point B , (Θ_+, P_+) , it jumps to B' after $+K_r$, which also sits in the basin of P_+ . Hence, stroboscopically, the rotor actually remains unchanged. Consequently, the following transition rules are achieved: $P_- \rightarrow P_0 \rightarrow P_+ \rightarrow P_+$, cf. blue lines in Fig. 1 (b). In other words, the system absorbs the input momentum from the drive, unless the rotor already has a maximum momentum, in which case the excess momentum is damped. A similar effect occurs for a negative kick $-K_r$: $P_+ \rightarrow P_0 \rightarrow P_- \rightarrow P_-$.

We employ this set of transition rules to realize the time rondeau order. The key is to introduce a dipolar structure to the random kick, i.e., at two consecutive stroboscopic times we randomly select one of the two kick sequences, $(+K_r, -K_r)$ or $(-K_r, +K_r)$. To see its dynamical consequences, we consider a simple yet insightful scenario where a single rotor starts from the initial condition $p(0)=0, \theta(0)=0$. As illustrated in Fig. 1 (c), after this dipolar kick the rotor always returns to its origin, establishing a long-time order, while the rotor can traverse multiple pathways, either $P_0 \rightarrow P_+ \rightarrow P_0$ or $P_0 \rightarrow P_- \rightarrow P_0$, demonstrating a short-time disorder. A typical trajectory is plotted in Fig. 2 in red.

Remarkably, regardless of the initial condition of the system, the rondeau order always appears at long times. This can be revealed by considering an ensemble of uncoupled rotors, starting from an arbitrary distribution of three fixed points, $\mathbf{W}(0)$. Its stroboscopic evolution can be obtained by $\mathbf{W}(2mT+2T) = \mathbf{A}\mathbf{W}(2mT)$ with a stochastic matrix of the Markovian chain [76]

$$\mathbf{A} = \begin{pmatrix} 1/2 & & \\ 1/2 & 1 & 1/2 \\ & & 1/2 \end{pmatrix}, \quad (2)$$

where the matrix elements $A_{i,j}$ denote the probability of updating the momentum from the i -th to j -th fixed points after one dipolar kick. Note, this dynamical system has a unique feature that if the momentum at time $2mT$ deviates from P_0 , the system always has the proba-

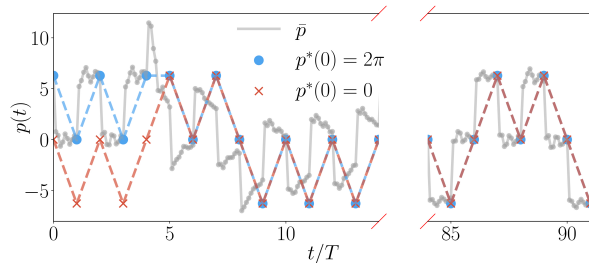


FIG. 2. Red and blue trajectories of a single rotor quickly synchronize, exhibiting the time rondeau order where the long-time order at $t=2mT$ coexists with the short-time disorder. The gray line depicts the average momentum in a many-rotor system, which follows the single-rotor trajectory. We use $J=0.25$, $K_r=5.5$ for the numerical simulation. The initial θ_i is randomly sampled within $[0, 2\pi]$ and p_i is sampled around P_+ according to a Gaussian distribution of a standard deviation 0.1.

bility of $1/2$ to correct it back to P_0 after one dipolar kick. Hence, the system exponentially converges to the stationary solution within four stroboscopic periods on average where the entire ensemble synchronizes and occupies P_0 at stroboscopic times [73]. As shown in Fig. 2, the blue trajectory quickly converges to the red one if their random kick sequences are the same, despite different initial conditions. Therefore, the transition rule (Fig. 1) provides exceptional stability for the rondeau order, which is robust against any initial state imperfections.

Many-body system with a finite waiting time.— The analysis above is exact only for uncoupled systems in the limit $T \rightarrow \infty$. Many-body interactions and a finite T inevitably introduce perturbations to the exact transition rule, potentially destabilizing the rondeau order. Yet, we will show that the TRC is indeed robust, and a de-synchronization phase transition occurs at a critical interaction strength in the thermodynamic limit.

To show this, we consider a many-rotor chain of size L with nearest-neighbor interactions, $H_I = -J \sum_i [\cos(\theta_i - \theta_{i+1}) + \cos(\theta_i - \theta_{i-1})] \sum_n \delta(t-n)$ with $J > 0$, resulting in

$$\begin{aligned} p_i(t+1) &= \gamma p_i(t) - K_0 \sin \theta_i(t) \pm K_r \delta_{t,mT} \\ &\quad + J[\sin(\theta_i(t) - \theta_{i+1}(t)) + \sin(\theta_i(t) - \theta_{i-1}(t))], \quad (3) \\ \theta_i(t+1) &= \theta_i(t) + p_i(t+1) \pmod{2\pi}, \end{aligned}$$

where i denotes the site number, \pm depends on the driving sequence being applied. In the following discussion, we fix $T=10$, which is far from the $T \rightarrow \infty$ limit even for the non-interacting limit, cf. details in the Appendix.

We first consider weak interaction strength and a spatially inhomogeneous initial state, where θ_i is randomly sampled within $[0, 2\pi]$ and p_i is sampled around a fixed point according to a Gaussian distribution. As shown in Fig. 2, at early times ($t/T \in [4, 11]$) the mean angular momentum $\bar{p} = \sum_i p_i / L$ (grey) exhibits a notable deviation from the exact single-rotor trajectory p^* at stroboscopic times (blue), while \bar{p} starts to follow p^* at longer times. We define $\mathcal{O}_{\bar{p}}(m) = [\bar{p}(mT) - p^*(m)]^2$, which quantifies

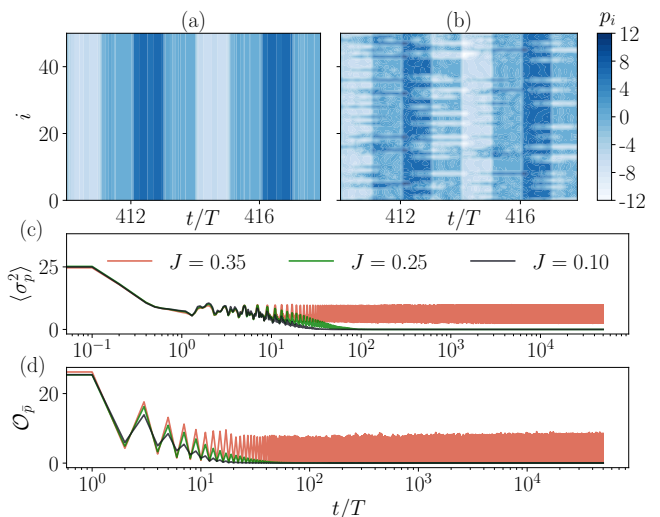


FIG. 3. (a) Spatial-temporal distribution of momentum in the synchronized phase for weak $J=0.25$. (b) Defects persist for stronger interaction $J=0.35$. Both (a) and (b) use the same random kick sequence. (c) and (d) Momentum variance and time rondeau order parameter for different J . Ensemble averages over different initial states and random drive realizations are performed. The system demonstrates synchronized TRC for a weak interaction (black and green) while a larger interaction induces de-synchronization (red). The initial momentum is sampled from a Gaussian distribution with a standard deviation 6 and zero average. We use parameters $K_r = 5.5$, $L = 256$ and a periodic boundary condition for numerical simulations.

their deviation as the TRC order parameter. As shown in Fig. 3(d), indeed, $\mathcal{O}_{\bar{p}}$ decays to zero (green and black), confirming the appearance of TRC in the presence of many-body interactions.

At long times, all rotors synchronize and become spatially ordered just as in the non-interacting case, where the system develops a homogeneous distribution of angular momentum, cf. Fig. 3(a). This can be confirmed via the spatial variance $\sigma_p^2 = \sum_{i=1}^L (p_i - \bar{p})^2 / L$. As shown in Fig. 3(c), after a short transient regime, the ensemble-averaged value $\langle \sigma_p^2 \rangle$ eventually drops to zero (black and green). Such a decay occurs exponentially fast in time, and the corresponding time scale τ converges to a finite value as long as L is sufficiently large, as detailed in Sec. SM 1, confirming that such a synchronized TRC remains stable in the thermodynamic limit.

Crucially, we note that for larger J this time scale also increases, cf. Fig. 3(c). This happens because a stronger interaction can maintain and even enhance the spatial inhomogeneity, via generating defects on top of the synchronized background, Fig. 3(b). Hence, in general, it takes a longer time for dissipation to stabilize the system. Perfect synchronization breaks down for large J and a finite-size system may exhibit intermittent synchronization [77], where the full synchronization and non-synchronized dynamics alternate irregularly in time, cf.

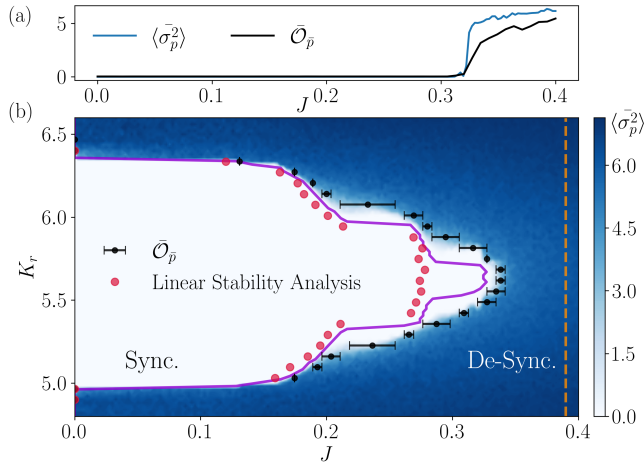


FIG. 4. (a) Dependence of order parameters on J for $K_r=5.5$. The de-synchronization phase transition occurs at $J_c \approx 0.32$. (b) Phase diagram for different K_r and J . White and blue regions correspond to the synchronization and de-synchronization phases, respectively. The purple curve corresponds to $\langle \bar{\sigma}_p^2 \rangle = 10^{-5}$. A linear stability analysis captures the phase transition (red). $T \rightarrow \infty$ assumption predicts $J_c \approx 0.39$ (orange), which overestimates the phase boundary. The black dots denote the phase boundary obtained by $\bar{\mathcal{O}}_{\bar{p}}$. Initial state distribution is the same as in Fig. 3.

Sec. SM 1. Yet, when $L \rightarrow \infty$, intermittent synchronization is unstable and the de-synchronization phase transition occurs at a critical value J_c . A finite density of defects survives indefinitely in the de-synchronization phase with non-vanishing spatial fluctuations, while the ron-deau order diminishes with non-zero $\bar{\mathcal{O}}_{\bar{p}}$ at long times, see red curves in Fig. 3 (c) and (d).

In Fig. 4 (a), we plot the long-time saturation value $\langle \bar{\sigma}_p^2 \rangle$ of the momentum variance and $\bar{\mathcal{O}}_{\bar{p}}$ for different J and the phase transition occurs around $J_c \approx 0.32$ when $K_r=5.5$ [78]. The phase transition point shows no dependence on the initial states, as synchronization occurs at early times, cf. Sec. SM 2 for the numerical verification. We further scan over a wide range of the random kick strengths K_r and J and map out the phase diagram in Fig. 4 (b): white and blue regions correspond to the synchronization ($\langle \bar{\sigma}_p^2 \rangle = 0$) and de-synchronization phases ($\langle \bar{\sigma}_p^2 \rangle \neq 0$), respectively, and the purple line corresponds to $\langle \bar{\sigma}_p^2 \rangle = 10^{-5}$. Black dots correspond to the average of three J values such that the order parameter $\bar{\mathcal{O}}_{\bar{p}}$ equals 0.2, 1.1 and 2, which match with the purple curve with good accuracy.

Linear Stability Analysis.— The de-synchronization phase transition can be well captured by a linear stability analysis (red dots in Fig. 4 (b)). The synchronized evolution can be captured by a mean-field solution $(\bar{p}(t), \bar{\theta}(t))$, i.e., the spatial average of momentum and angle which follow the single-rotor EOM, Eq. (1). Many-body interactions generate spatial fluctuations, $\Delta\theta_i(t) = \theta_i(t) - \bar{\theta}(t)$ and $\Delta p_i(t) = p_i(t) - \bar{p}(t)$. We as-

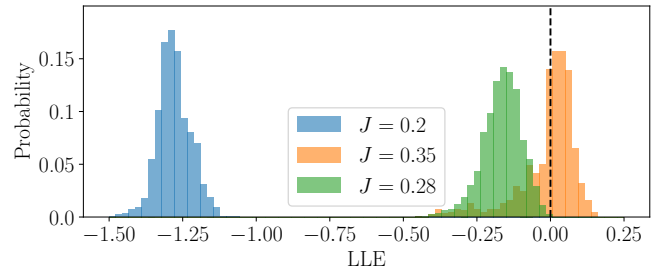


FIG. 5. Distribution of largest Lyapunov exponents (LLEs). We consider a de-synchronization phase transition occurs when 5% of LLEs become positive. Numerically we use $K_r=5.5, m=300$ and 1000 different mean-field trajectories. Convergence of the distribution is discussed in Sec. SM 3.

sume $\Delta\theta_i(t) \ll 1$, $\Delta p_i(t) \ll 1$ and only keep its leading order contributions to Eq. (3), $\Delta p_i(t+1) = \gamma \Delta p_i(t) - K_0 \cos \bar{\theta}(t) \Delta\theta_i(t) + J[2\Delta\theta_i(t) - \Delta\theta_{i+1}(t) - \Delta\theta_{i-1}(t)]$, $\Delta\theta_i(t+1) = \Delta\theta_i(t) + \Delta p_i(t+1) \pmod{2\pi}$. A Fourier transformation, $\Delta p_k(t) = \sum_j \Delta p_j e^{-ij k} / \sqrt{N}$ and $\Delta\theta_k(t) = \sum_j \Delta\theta_j e^{-ij k} / \sqrt{N}$, leads to the decoupled EOMs

$$\begin{pmatrix} \Delta p_k(t+1) \\ \Delta\theta_k(t+1) \end{pmatrix} = \mathbf{A}_k(t) \begin{pmatrix} \Delta p_k(t) \\ \Delta\theta_k(t) \end{pmatrix}, \quad (4)$$

for each quasi-momentum k mode with the Jacobian matrix

$$\mathbf{A}_k(\bar{\theta}(t)) = \begin{pmatrix} \gamma & 2J(1 - \cos(k)) - K_0 \cos \bar{\theta}(t) \\ \gamma & 1 + 2J(1 - \cos(k)) - K_0 \cos \bar{\theta}(t) \end{pmatrix}. \quad (5)$$

The dependence on the random kick sequence and K_r are entirely contained in $\bar{\theta}(t)$ and \mathbf{A}_k varies in time.

For simplicity, we first consider the limit $T \rightarrow \infty$, where the transition rules are exact, and $(\bar{p}(t), \bar{\theta}(t))$ only has three possible choices - three fixed points. The stability of this mean-field solution can be determined by all the eigenvalues λ_k of \mathbf{A}_k for each fixed point: If $\max |\lambda_k| < 1$ for all k , the trajectory is stable and fluctuations eventually vanish. Larger J may generate unstable k modes with $|\lambda_k| > 1$ and the critical value is determined when $\max |\lambda_k(J_c)| = 1$. This leads to the orange line in Fig. 4, however, it notably overestimates J_c . Crucially, the dependence of J_c on the random kick strength K_r cannot be captured.

A finite T plays a crucial role in determining the TRC stability and the deviation between $(\bar{p}(t), \bar{\theta}(t))$ and the fixed points cannot be neglected. We define \mathbf{D}_k as the product of \mathbf{A}_k calculated along a mean-field trajectory $\bar{\theta}(t)$ [79] during m dipolar drives $\mathbf{D}_k = \prod_{i=0}^{2mT-1} \mathbf{A}_k(\bar{\theta}(i))$. For a given trajectory, we obtain the eigenvalues λ_k of \mathbf{D}_k and the corresponding largest Lyapunov exponents (LLEs), $\lim_{m \rightarrow \infty} \log(\max |\lambda_k|) / m$, can be obtained. In Fig. 5, we plot the distribution of LLEs for different mean-field trajectories. In the synchronization phase (blue) LLEs are negative, while for large J a notable fraction of LLEs become positive. We estimate the critical J_c when 5% of LLEs become positive, and as shown in

Fig. 4(b), the result matches well with the phase boundary obtained by the many-body simulation.

Discussion.— Our work opens a promising new avenue for stabilizing the partial temporal order via dissipation, demonstrating the existence of TRCs that are absolutely stable against perturbations in both initial states and many-body interactions. One important ingredient is multistability, such that the system jumps among different fixed points without generating unwanted heating. A dipolar structure encodes the rondeau order and synchronization notably strengthens its stability.

Going beyond, dissipative systems can exhibit a versatile structure of stationary states, such as limit cycles [50] and (quasi-)periodic orbits [54] in addition to the fixed points considered here. We expect that the partial temporal order can be significantly enriched in these settings. It is worth noting that the dipolar structure can be straightforwardly extended to higher-order multipoles and the aperiodic Thue-Morse sequence [18]. We anticipate enhanced stability of the synchronized TRCs for higher multipolar orders and a systematic study would be worth pursuing.

The presence of many-body interactions sustains spatially inhomogeneous defects. Its competition with the synchronized dynamics leads to the de-synchronization phase transition. We perform large-scale and long-time numerical simulations of the classical many-body dynam-

ics. It allows us to map out the entire phase diagram and explore the robustness of TRCs against perturbations.

While we have demonstrated stable TRCs in classical many-body systems for numerical efficiency, our construction is readily generalizable to quantum systems, where both multistability [60, 64, 80] and synchronization have been reported [72, 74, 81]. It remains an interesting question to investigate the competition between quantum fluctuations and synchronization, which may induce non-equilibrium quantum phase transitions that are fundamentally different. As detailed in Sec. SM 4, our rotor system can be experimentally implemented on the superconducting quantum simulation platform [33, 82]. Such a system may serve as a natural testbed to reveal distinct behaviors in the non-equilibrium temporal order between classical and quantum systems.

Acknowledgments.— This work is supported by the National Natural Science Foundation of China (Grants No. 12234002, 12474214, 12474486, and 92250303), by the National Key Research and Development Program of China (Grant No. 2024YFA1612101), and by “The Fundamental Research Funds for the Central Universities, Peking University” and “High-performance Computing Platform of Peking University”. We thank Johannes Knolle for initiating this work and stimulating discussions. We also thank Marin Bukov for many useful discussions.

-
- [1] V. Khemani, A. Lazarides, R. Moessner, and S. L. Sondhi, Phase structure of driven quantum systems, *Phys. Rev. Lett.* **116**, 250401 (2016).
- [2] D. V. Else, B. Bauer, and C. Nayak, Floquet time crystals, *Phys. Rev. Lett.* **117**, 090402 (2016).
- [3] N. Y. Yao, A. C. Potter, I.-D. Potirniche, and A. Vishwanath, Discrete time crystals: Rigidity, criticality, and realizations, *Phys. Rev. Lett.* **118**, 030401 (2017).
- [4] A. Verdeny, J. Puig, and F. Mintert, Quasi-periodically driven quantum systems, *Zeitschrift für Naturforschung A* **71**, 897 (2016).
- [5] S. Nandy, A. Sen, and D. Sen, Aperiodically driven integrable systems and their emergent steady states, *Phys. Rev. X* **7**, 031034 (2017).
- [6] T. Mori, H. Zhao, F. Mintert, J. Knolle, and R. Moessner, Rigorous bounds on the heating rate in thue-morse quasiperiodically and randomly driven quantum many-body systems, *Phys. Rev. Lett.* **127**, 050602 (2021).
- [7] X. Wen, R. Fan, A. Vishwanath, and Y. Gu, Periodically, quasiperiodically, and randomly driven conformal field theories, *Phys. Rev. Res.* **3**, 023044 (2021).
- [8] D. M. Long, P. J. Crowley, and A. Chandran, Many-body localization with quasiperiodic driving, *Phys. Rev. B* **105**, 144204 (2022).
- [9] G. He, B. Ye, R. Gong, Z. Liu, K. W. Murch, N. Y. Yao, and C. Zu, Quasi-floquet prethermalization in a disordered dipolar spin ensemble in diamond, *Phys. Rev. Lett.* **131**, 130401 (2023).
- [10] M. Gallone and B. Langella, Prethermalization and conservation laws in quasi-periodically driven quantum systems, *Journal of Statistical Physics* **191**, 100 (2024).
- [11] S. Ghosh, S. Bhattacharjee, and S. Bandyopadhyay, Slow relaxation of quasi-periodically driven integrable quantum many-body systems, *arXiv preprint arXiv:2404.06667* (2024).
- [12] H. Schmid, Y. Peng, G. Refael, and F. von Oppen, Self-similar phase diagram of the fibonacci-driven quantum ising model, *arXiv preprint arXiv:2410.18219* (2024).
- [13] P. T. Dumitrescu, R. Vasseur, and A. C. Potter, Logarithmically slow relaxation in quasiperiodically driven random spin chains, *Phys. Rev. Lett.* **120**, 070602 (2018).
- [14] H. Zhao, F. Mintert, and J. Knolle, Floquet time spirals and stable discrete-time quasicrystals in quasiperiodically driven quantum many-body systems, *Phys. Rev. B* **100**, 134302 (2019).
- [15] D. V. Else, W. W. Ho, and P. T. Dumitrescu, Long-lived interacting phases of matter protected by multiple time-translation symmetries in quasiperiodically driven systems, *Phys. Rev. X* **10**, 021032 (2020).
- [16] H. Zhao, J. Knolle, and R. Moessner, Temporal disorder in spatiotemporal order, *Phys. Rev. B* **108**, L100203 (2023).
- [17] L. J. I. Moon, P. M. Schindler, Y. Sun, E. Druga, J. Knolle, R. Moessner, H. Zhao, M. Bukov, and A. Ajoy, Experimental observation of a time rondeau crystal: Temporal disorder in spatiotemporal order, *arXiv preprint arXiv:2404.05620* (2024).
- [18] H. Zhao, F. Mintert, R. Moessner, and J. Knolle, Random multipolar driving: Tunably slow heating through spectral engineering, *Phys. Rev. Lett.* **126**, 040601 (2021).

- (2021).
- [19] X. Wen, Y. Gu, A. Vishwanath, and R. Fan, Periodically, quasi-periodically, and randomly driven conformal field theories (ii): Furstenberg’s theorem and exceptions to heating phases, *SciPost Physics* **13**, 082 (2022).
- [20] J. Yan, R. Moessner, and H. Zhao, Prethermalization in aperiodically kicked many-body dynamics, *Phys. Rev. B* **109**, 064305 (2024).
- [21] V. Tiwari, D. S. Bhakuni, and A. Sharma, Dynamical localization and slow dynamics in quasiperiodically driven quantum systems, *Phys. Rev. B* **109**, L161104 (2024).
- [22] E. Levi, M. Heyl, I. Lesanovsky, and J. P. Garrahan, Robustness of many-body localization in the presence of dissipation, *Phys. Rev. Lett.* **116**, 237203 (2016).
- [23] S. Gopalakrishnan, K. R. Islam, and M. Knap, Noise-induced subdiffusion in strongly localized quantum systems, *Phys. Rev. Lett.* **119**, 046601 (2017).
- [24] M.-T. Rieder, L. M. Sieberer, M. H. Fischer, and I. C. Fulga, Localization counteracts decoherence in noisy floquet topological chains, *Phys. Rev. Lett.* **120**, 216801 (2018).
- [25] H. Zhao, F. Mintert, J. Knolle, and R. Moessner, Localization persisting under aperiodic driving, *Phys. Rev. B* **105**, L220202 (2022).
- [26] A. Lazarides, A. Das, and R. Moessner, Equilibrium states of generic quantum systems subject to periodic driving, *Phys. Rev. E* **90**, 012110 (2014).
- [27] H. Kim, T. N. Ikeda, and D. A. Huse, Testing whether all eigenstates obey the eigenstate thermalization hypothesis, *Phys. Rev. E* **90**, 052105 (2014).
- [28] L. D’Alessio and M. Rigol, Long-time Behavior of Isolated Periodically Driven Interacting Lattice Systems, *Phys. Rev. X* **4**, 041048 (2014).
- [29] M. Bukov, S. Gopalakrishnan, M. Knap, and E. Demler, Prethermal floquet steady states and instabilities in the periodically driven, weakly interacting bose-hubbard model, *Phys. Rev. Lett.* **115**, 205301 (2015).
- [30] T. Kuwahara, T. Mori, and K. Saito, Floquet–magnus theory and generic transient dynamics in periodically driven many-body quantum systems, *Annals of Physics* **367**, 96 (2016).
- [31] D. V. Else, B. Bauer, and C. Nayak, Prethermal phases of matter protected by time-translation symmetry, *Phys. Rev. X* **7**, 011026 (2017).
- [32] T. Mori, Floquet prethermalization in periodically driven classical spin systems, *Phys. Rev. B* **98**, 104303 (2018).
- [33] A. Rajak, I. Dana, and E. G. Dalla Torre, Characterizations of prethermal states in periodically driven many-body systems with unbounded chaotic diffusion, *Phys. Rev. B* **100**, 100302 (2019).
- [34] O. Howell, P. Weinberg, D. Sels, A. Polkovnikov, and M. Bukov, Asymptotic prethermalization in periodically driven classical spin chains, *Phys. Rev. Lett.* **122**, 010602 (2019).
- [35] D. J. Luitz, R. Moessner, S. Sondhi, and V. Khemani, Prethermalization without temperature, *Phys. Rev. X* **10**, 021046 (2020).
- [36] A. Rubio-Abadal, M. Ippoliti, S. Hollerith, D. Wei, J. Rui, S. Sondhi, V. Khemani, C. Gross, and I. Bloch, Floquet prethermalization in a bose-hubbard system, *Phys. Rev. X* **10**, 021044 (2020).
- [37] A. Pizzi, A. Nunnenkamp, and J. Knolle, Classical prethermal phases of matter, *Phys. Rev. Lett.* **127**, 140602 (2021).
- [38] B. Ye, F. Machado, and N. Y. Yao, Floquet phases of matter via classical prethermalization, *Phys. Rev. Lett.* **127**, 140603 (2021).
- [39] P. Peng, C. Yin, X. Huang, C. Ramanathan, and P. Capellaro, Floquet prethermalization in dipolar spin chains, *Nature Physics* **17**, 444 (2021).
- [40] C. Fleckenstein and M. Bukov, Thermalization and prethermalization in periodically kicked quantum spin chains, *Phys. Rev. B* **103**, 144307 (2021).
- [41] T. N. Ikeda and A. Polkovnikov, Fermi’s golden rule for heating in strongly driven floquet systems, *Phys. Rev. B* **104**, 134308 (2021).
- [42] M. H. Muñoz Arias, K. Chinni, and P. M. Poggi, Floquet time crystals in driven spin systems with all-to-all p -body interactions, *Phys. Rev. Res.* **4**, 023018 (2022).
- [43] W. Beatrez, C. Fleckenstein, A. Pillai, E. de Leon Sanchez, A. Akkiraju, J. Diaz Alcalá, S. Conti, P. Reshetikhin, E. Druga, M. Bukov, *et al.*, Critical prethermal discrete time crystal created by two-frequency driving, *Nature Physics* **19**, 407 (2023).
- [44] H.-K. Jin, J. Knolle, and M. Knap, Fractionalized prethermalization in a driven quantum spin liquid, *Phys. Rev. Lett.* **130**, 226701 (2023).
- [45] W. W. Ho, T. Mori, D. A. Abanin, and E. G. Dalla Torre, Quantum and classical floquet prethermalization, *Annals of Physics* **454**, 169297 (2023).
- [46] M. Yue and Z. Cai, Prethermal time-crystalline spin ice and monopole confinement in a driven magnet, *Phys. Rev. Lett.* **131**, 056502 (2023).
- [47] Y. Hou, Z. Fu, R. Moessner, M. Bukov, and H. Zhao, Floquet-engineered emergent massive nambu-goldstone modes, [arXiv preprint arXiv:2409.01902](https://arxiv.org/abs/2409.01902) (2024).
- [48] Z. Fu, R. Moessner, H. Zhao, and M. Bukov, Engineering hierarchical symmetries, *Phys. Rev. X* **14**, 041070 (2024).
- [49] H.-Y. Qi, Y. Wu, and W. Zheng, Topological origin of floquet thermalization in periodically driven many-body systems, [arXiv preprint arXiv:2404.18052](https://arxiv.org/abs/2404.18052) (2024).
- [50] F. Piazza and H. Ritsch, Self-ordered limit cycles, chaos, and phase slippage with a superfluid inside an optical resonator, *Phys. Rev. Lett.* **115**, 163601 (2015).
- [51] B. Buča, J. Tindall, and D. Jaksch, Non-stationary coherent quantum many-body dynamics through dissipation, *Nature Communications* **10**, 1730 (2019).
- [52] T. Mori, Floquet states in open quantum systems, *Annual Review of Condensed Matter Physics* **14**, 35 (2023).
- [53] K. Kawabata, A. Kulkarni, J. Li, T. Numasawa, and S. Ryu, Symmetry of open quantum systems: Classification of dissipative quantum chaos, *PRX Quantum* **4**, 030328 (2023).
- [54] A. Russomanno, Spatiotemporally ordered patterns in a chain of coupled dissipative kicked rotors, *Phys. Rev. B* **108**, 094305 (2023).
- [55] S. Yi-Thomas and J. D. Sau, Theory for dissipative time crystals in coupled parametric oscillators, *Phys. Rev. Lett.* **133**, 266601 (2024).
- [56] Z. Gong, R. Hamazaki, and M. Ueda, Discrete Time-Crystalline Order in Cavity and Circuit QED Systems, *Phys. Rev. Lett.* **120**, 040404 (2018).
- [57] F. Iemini, A. Russomanno, J. Keeling, M. Schirò, M. Dalmonte, and R. Fazio, Boundary time crystals, *Phys. Rev. Lett.* **121**, 035301 (2018).
- [58] H. Keßler, P. Kongkhambut, C. Georges, L. Mathey, J. G. Cosme, and A. Hemmerich, Observation of a dissipative time crystal, *Phys. Rev. Lett.* **127**, 043602 (2021).

- [59] X. Wu, Z. Wang, F. Yang, R. Gao, C. Liang, M. K. Tey, X. Li, T. Pohl, and L. You, Dissipative time crystal in a strongly interacting rydberg gas, *Nature Physics* **20**, 1389 (2024).
- [60] P. Solanki, M. Krishna, M. Hajdušek, C. Bruder, and S. Vinjanampathy, Exotic synchronization in continuous time crystals outside the symmetric subspace, *Phys. Rev. Lett.* **133**, 260403 (2024).
- [61] N. Y. Yao, C. Nayak, L. Balents, and M. P. Zaletel, Classical discrete time crystals, *Nature Physics* **16**, 438 (2020).
- [62] S. Boccaletti, J. Kurths, G. Osipov, D. Valladares, and C. Zhou, The synchronization of chaotic systems, *Physics reports* **366**, 1 (2002).
- [63] A. N. Pisarchik and U. Feudel, Control of multistability, *Physics Reports* **540**, 167 (2014).
- [64] H. Landa, M. Schiró, and G. Misguich, Multistability of driven-dissipative quantum spins, *Phys. Rev. Lett.* **124**, 043601 (2020).
- [65] H. Alaeian and B. Buča, Exact multistability and dissipative time crystals in interacting fermionic lattices, *Communications Physics* **5**, 318 (2022).
- [66] G. M. Zaslavsky, The simplest case of a strange attractor, *Physics Letters A* **69**, 145 (1978).
- [67] K. Matsumoto and I. Tsuda, Noise-induced order, *Journal of Statistical Physics* **31**, 87 (1983).
- [68] C. Van den Broeck, J. M. R. Parrondo, and R. Toral, Noise-induced nonequilibrium phase transition, *Phys. Rev. Lett.* **73**, 3395 (1994).
- [69] C. Zhou and J. Kurths, Noise-induced phase synchronization and synchronization transitions in chaotic oscillators, *Phys. Rev. Lett.* **88**, 230602 (2002).
- [70] J.-n. Teramae and D. Tanaka, Robustness of the noise-induced phase synchronization in a general class of limit cycle oscillators, *Phys. Rev. Lett.* **93**, 204103 (2004).
- [71] D. S. Goldobin and A. Pikovsky, Synchronization and desynchronization of self-sustained oscillators by common noise, *Phys. Rev. E* **71**, 045201 (2005).
- [72] I. Goychuk, J. Casado-Pascual, M. Morillo, J. Lehmann, and P. Hänggi, Quantum stochastic synchronization, *Phys. Rev. Lett.* **97**, 210601 (2006).
- [73] W. Huang, H. Qian, S. Wang, F. X.-F. Ye, and Y. Yi, Synchronization in discrete-time, discrete-state random dynamical systems, *SIAM Journal on Applied Dynamical Systems* **19**, 233 (2020).
- [74] F. Schmolke and E. Lutz, Noise-induced quantum synchronization, *Phys. Rev. Lett.* **129**, 250601 (2022).
- [75] We discuss different parameter regimes and the stability of the transition rule in the Appendix.
- [76] S. P. Meyn and R. L. Tweedie, *Markov chains and stochastic stability* (Springer Science & Business Media, 2012).
- [77] A. Berger, H. Qian, S. Wang, and Y. Yi, Intermittent synchronization in finite-state random networks under markov perturbations, *Communications in Mathematical Physics* **384**, 1945 (2021).
- [78] Long-time saturation values are obtained by averaging order parameters at 8 stroboscopic times, starting from $t = 10^5$.
- [79] A. Wolf, J. B. Swift, H. L. Swinney, and J. A. Vastano, Determining lyapunov exponents from a time series, *Physica D: nonlinear phenomena* **16**, 285 (1985).
- [80] Y. Xu, F.-X. Sun, W. Zhang, Q. He, and H. Pu, Phase transition and multistability in dicke dimer, *Phys. Rev. Lett.* **133**, 233604 (2024).
- [81] M. Xu, D. A. Tieri, E. C. Fine, J. K. Thompson, and M. J. Holland, Synchronization of two ensembles of atoms, *Phys. Rev. Lett.* **113**, 154101 (2014).
- [82] F. S. Cataliotti, S. Burger, C. Fort, P. Maddaloni, F. Minardi, A. Trombettoni, A. Smerzi, and M. Inguscio, Josephson Junction Arrays with Bose-Einstein Condensates, *Science* **293**, 843 (2001).

End Matter

Appendix.— In the absence of many-body interactions, an ensemble of kicked rotors can exhibit various types of dynamics that depend on both the waiting time T and the random kick strength K_r . For $T \rightarrow \infty$, as elaborated in the main text, the system exhibits the time rondeau order and synchronization protects it against initial state perturbations. Here, we show that this phenomenon indeed persists for finite T , and we depict the entire phase diagram in Fig. 6.

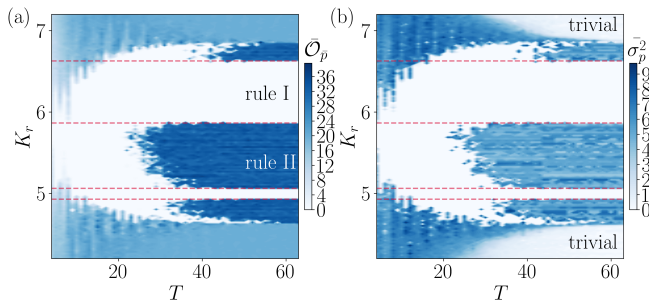


FIG. 6. Phase diagram for the single-rotor system for different waiting time T and random drive strength K_r . The order parameter \bar{O}_p and the variance of momentum $\bar{\sigma}_p^2$ are plotted in (a) and (b), respectively. We average over 10 stroboscopic times around $t = 2 \times 10^4$ to obtain their long time saturation values. “Rule I” corresponds to the synchronized time rondeau order. “Rule II” and other trivial phases are discussed in the text. Rule I and II are separated by red lines when T is sufficiently large. These phase boundaries are obtained by analyzing the basin structure of the periodically kicked rotors when $T \rightarrow \infty$, but it can still capture the phase boundary for a large range of T . When T is further reduced, e.g. $T \approx 20$, Rule I remains remarkably stable but Rule II no longer persists. The initial conditions of momenta have Gaussian distributions with zero average and standard deviation $\sigma_p = 6$.

We numerically obtain two order parameters at long times: \bar{O}_p , the deviation from the perfect rondeau evolution for $T \rightarrow \infty$ and the fluctuation of the momentum of the entire rotor ensemble, $\bar{\sigma}_p^2$. There are four possible phases as shown in Fig. 6:

- The synchronized time rondeau, induced by Transition Rule I (Fig. 1(b) in the main text) appears when both order parameters vanish (white region).
- The light blue region in Fig. 6(a) corresponds to the random motion that exhibits neither the rondeau order nor the synchronized behavior.
- The dark blue regions in Fig. 6(a) correspond to dynamics induced by Transition Rule II, which will be explained in detail later.
- In the “trivial” region (white in Fig. 6(b)), rotors rapidly synchronize since they relax to the fixed

point P_0 . Hence, no stroboscopic transition between fixed points can exist, and \bar{O}_p remains finite.

Transition rule I.—For large T , the stroboscopic transition rule can be precisely determined by analyzing the structure of the basins of fixed points as shown in Fig. 1(a). To realize Transition Rule I, we numerically find that the strength K_r should be in the region $(4.93, 5.06) \cup (5.87, 6.63)$ so that a positive kick can drive points A and B to the blue region (the basin of the fixed point P_+) simultaneously. We plot the boundaries of K_r as red dashed lines in Fig. 6, which precisely capture the phase boundary of Rule I when T is sufficiently large.

Transition rule II.— When K_r lies in the parameter region $(4.63, 4.93) \cup (5.06, 5.86) \cup (6.63, 6.85)$, different stroboscopic dynamics can appear in the limit of $T \rightarrow \infty$

$$\begin{aligned} +K_r : P_+ &\rightarrow P_0 & P_0 &\rightarrow P_+ & P_- &\rightarrow P_0 \\ -K_r : P_+ &\rightarrow P_0 & P_0 &\rightarrow P_- & P_- &\rightarrow P_0, \end{aligned} \quad (6)$$

which we dub as Rule II. This type of dynamics appears in the dark blue regions in Fig. 6(a). The only difference from Rule I is $P_+ \rightarrow P_0$ for a positive kick and $P_- \rightarrow P_0$ for a negative kick.

The dynamics after a dipolar kick can also be analyzed via a Markovian process. The corresponding stochastic matrix reads

$$\mathbf{A} = \begin{pmatrix} 1/2 & 1/2 \\ 1/2 & 1/2 \end{pmatrix}, \quad (7)$$

and by diagonalizing this matrix, we find that it has two invariant subspaces spanned by \vec{e}_2 and $\{\vec{e}_1 + \vec{e}_3, \vec{e}_1 - \vec{e}_3\}$, where, for example, $\vec{e}_1 = (1, 0, 0)^T$ is a unit base vector. These two subspaces correspond to two possible motions. \vec{e}_2 corresponds to Motion I, where the rotor always stays at the fixed point P_0 at time $2mT$,

$$\begin{aligned} (+K_r, -K_r) : P_0 &\rightarrow P_+ \rightarrow P_0, \\ (-K_r, +K_r) : P_0 &\rightarrow P_- \rightarrow P_0, \end{aligned} \quad (8)$$

which also reproduces the synchronized steady state as in the main text. In contrast, in the subspace spanned by $\{\vec{e}_1 + \vec{e}_3, \vec{e}_1 - \vec{e}_3\}$, Motion II appears

$$\begin{aligned} (+K_r, -K_r) : P_+ &\rightarrow P_0 \rightarrow P_-, & P_- &\rightarrow P_0 \rightarrow P_-, \\ (-K_r, +K_r) : P_+ &\rightarrow P_0 \rightarrow P_+, & P_- &\rightarrow P_0 \rightarrow P_+, \end{aligned} \quad (9)$$

and the rotor jumps randomly between P_+ and P_- at time $2mT$. Therefore, rotors starting from different initial conditions will not synchronize and exhibit one of these two motions at long times.

Rotors starting from widely distributed initial conditions prefer Motion II in the large T limit. To see this, we first notice that the momentum difference at stroboscopic times between motion II and motion I is exact 2π . Also, the order parameter in the dark blue region in Fig. 6(a) is $\bar{O}_p \approx 4\pi^2$, suggesting that most rotors exhibit Motion II. Further, \bar{O}_p is large enough to distinguish Motion II from the light blue region, where rotors

exhibit a random motion. We can understand this phenomenon again by analyzing the basin structure shown in Fig. 1(a): Clearly, the area of the white region is larger than the blue or the red region. Hence, after the first stroboscopic kick, rotors with widely distributed initial conditions quickly converge to the fixed point P_0 within maximum probability and evolve according to Motion II afterward.

Finite T behavior.— When T is finite, analysis becomes complicated since one cannot construct the stochastic matrix according to the basin structure. Instead, we perform extensive numerical simulations to map out the phase diagram. We note that Rule I is remarkably stable and survives in a wide parameter space, while Rule II becomes unstable at a finite T . It remains an interesting open question to further justify the stability of Rule I, and we leave this to future work. In the current study, we fix $T = 10$, which is indeed far from the $T \rightarrow \infty$ limit, and focus on the stability of time roudau crystals in the presence of many-body interactions.

Supplementary Material
Stable time rondeau crystals in dissipative many-body systems

CONTENTS

SM 1. System size dependence of order parameters and intermittent synchronization	10
SM 2. Independence of initial conditions	11
SM 3. Convergence of the distribution of the largest Lyapunov exponents	12
SM 4. Experimental realization	12

SM 1. SYSTEM SIZE DEPENDENCE OF ORDER PARAMETERS AND INTERMITTENT SYNCHRONIZATION

In the main text, we demonstrate the existence of the synchronization phase in the presence of weak many-body interactions and a de-synchronization phase for large J . Here, we provide more numerical evidence to show these two phases are thermodynamically stable.

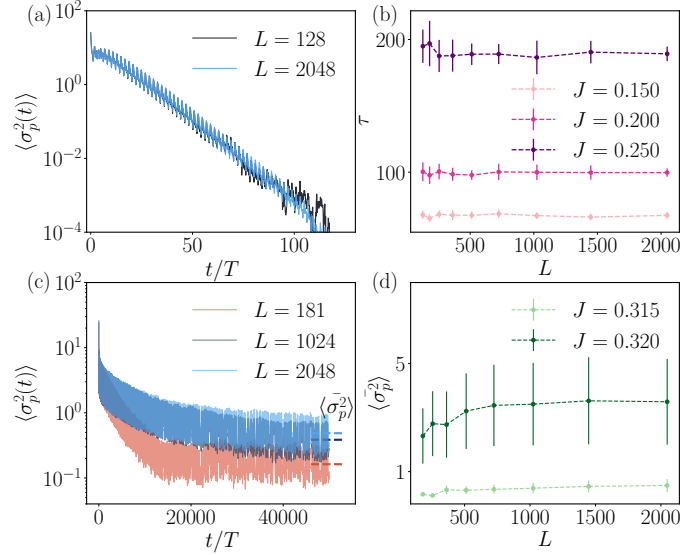


FIG. S1. (a) Synchronization occurs for weak interaction strength, where the momentum variance decays to zero exponentially fast in time. Finite-size effects only become visible at late times, e.g., $t \approx 80T$. Here we use $J = 0.2$. (b) The time scale τ before synchronization is independent of the system size. Longer time is needed for a larger interaction strength. (c) For $J > J_c$, de-synchronization occurs and the spatial fluctuation does not vanish. J_c is about 0.31. (d) The long-time average $\langle \sigma_p^2 \rangle$ (dashed line in (c)) converges for larger system sizes. The increase of J generally induces a larger spatial fluctuation. The initial momentum is sampled from a Gaussian distribution with a standard deviation of 6 and zero average. We use $K_r = 5.5$ for these numerical simulations.

As shown in Fig. S1(a), for weak interaction $J = 0.2$, the ensemble-averaged order parameter $\langle \sigma_p^2 \rangle$ decays to zero, suggesting that the synchronization phase is quickly established. By comparing the numerical simulation performed for different system sizes (black and blue lines), we conclude that such a decaying process is largely independent of L , and finite-size effects only appear at longer times, e.g., $t/T > 80$. Also, it occurs exponentially fast in time, $\langle \sigma_p^2 \rangle \propto e^{-t/\tau}$, and the corresponding synchronization time scale τ can be obtained by performing a linear fit in panel (a), where a log scale is used. In Fig. S1(b), we can see τ becomes independent of the system sizes for large L .

As we increase the interaction strength, τ also grows and a phase transition to de-synchronization occurs for large J . We extract the saturation value of the $\langle \sigma_p^2(t) \rangle$ at sufficiently long times (dashed lines in Fig. S1(c)). As shown in

Fig. S1(d), we illustrate its dependence on the system size, and clearly it converges to a non-vanishing value in the thermodynamic limit for $J > J_c$.

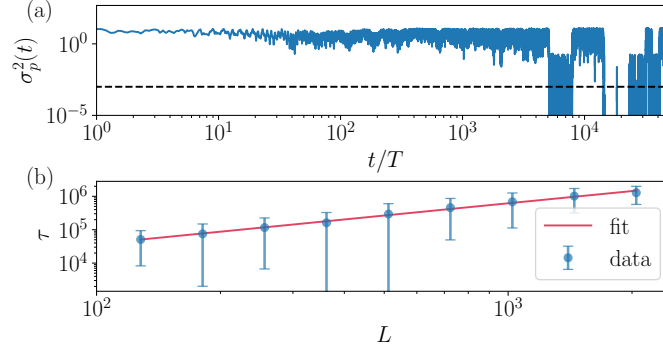


FIG. S2. (a) Intermittent synchronization when $J = 0.32, L = 128$. The dashed black line denotes $\sigma_p^2(t) = 10^{-3}$. (b) τ denotes the first time where the spatial fluctuation drops below the threshold value (black dashed line in (a)). It follows a power-law dependence on the system size. We use $J = 0.318$ for numerical simulation. For each system size, we simulate 112 trajectories to get the average value of τ and the error bar corresponds to the standard deviation.

Interestingly, as shown in Fig. S2(a), we notice that for a finite-size system, intermittent synchronization can occur near the phase transition point, where full synchronization and the non-synchronized dynamics alternate irregularly in time. However, this phenomenon is thermodynamically unstable. To show this, we use the threshold value 10^{-3} (dashed black line) and extract the synchronization time scale τ , after which the system's spatial fluctuation first drops below this threshold. We consider many different realizations and plot the mean value of τ versus different system sizes in Fig. S2(b), where the error bar denotes the standard deviation. We use a log-log scale in Fig. S2(b). Numerical results fit well with a straight line (red), suggesting a power law dependence of τ on size L . Therefore, we conclude that for large interaction strength J , intermittent synchronization will not occur in the thermodynamic limit for $L \rightarrow \infty$.

SM 2. INDEPENDENCE OF INITIAL CONDITIONS

The phase diagram Fig. 4 in the main text does not depend on the specific choices of initial conditions. In Fig. S3, we plot the order parameters for different J , calculated with different initial conditions. Small differences are observed in the de-synchronization phase, whereas the phase boundary remains unchanged.

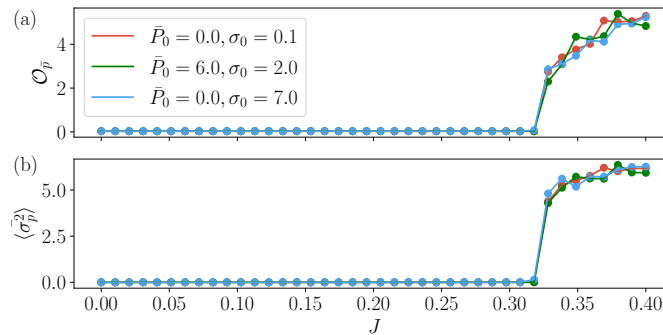


FIG. S3. The order parameters \mathcal{O}_p and $\langle \sigma_p^2 \rangle$ are independent of initial conditions. Here the evolution of the many-body system begins at a random Gaussian distribution of both momentum and angle for each site, exhibited in different colors. \bar{P}_0 is the average and σ_0 is the standard deviation of the Gaussian distribution for the initial momenta. The standard deviation of the initial angles is $\sigma = 3$. We use $K_r = 5.5, T = 10$, and $L = 100$ for numerical simulations and extract order parameters at $t/2T = 10^4$.

SM 3. CONVERGENCE OF THE DISTRIBUTION OF THE LARGEST LYAPUNOV EXPONENTS

The distribution of the largest Lyapunov exponents (LLE) converges when the number of dipolar kicks, m , is sufficiently large. To see this, we evolve 1000 single-rotor trajectories during m dipolar drives with a random Gaussian-distributed initial momentum, $\sigma_p^2 = 0.01$, $\bar{p} = 0$, and all the initial angles fixed at zero. For each mean-field trajectory $\{\bar{\theta}(t)\}$, we can compute a series of matrix products $\mathbf{D}_k = \prod_{i=0}^{2mT-1} \mathbf{A}_k(\bar{\theta}(i))$. Then the LLE of each trajectory can be calculated from its maximum eigenvalue. We present the histogram of all the LLEs of the synchronization and de-synchronization phases in Fig. S4(b) and Fig. S4(d), respectively. We notice that the distribution of LLEs sharpens, and crucially, the fraction of positive LLEs converges for larger m . To quantify this, we define ρ as the fraction of LLEs that become positive. Clearly, it quickly converges to zero in Fig. S4(a) but remains finite in (c), corresponding to the synchronization and de-synchronization phase. In the main text, we use $m = 300$ that is sufficiently large to capture the phase boundary.

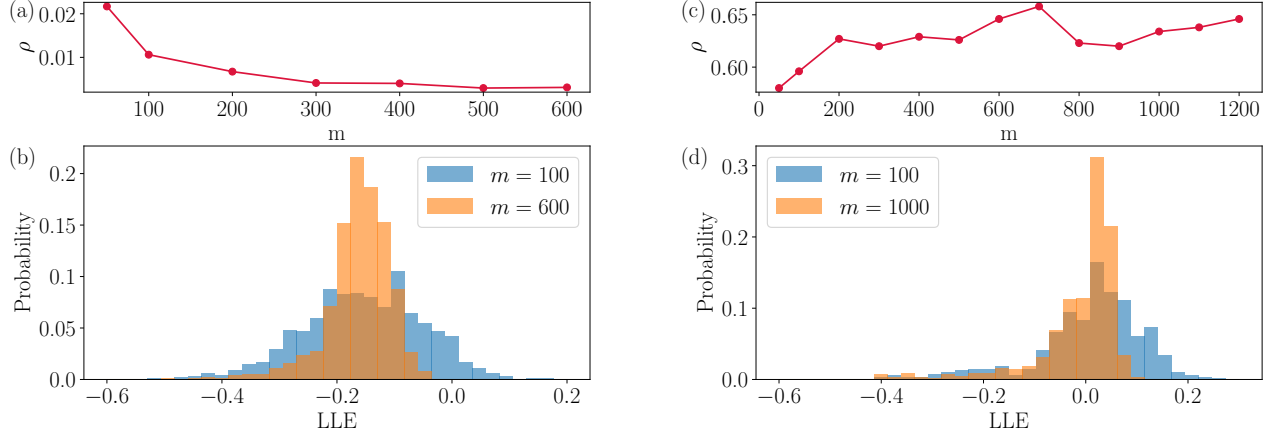


FIG. S4. (a)(c) ρ denotes the fraction of positive LLEs. As the number of dipolar kicks m increases, ρ converges to zero in panel (a), while it remains finite in panel (c), corresponding to the synchronization and de-synchronization phases, respectively. (b)(d) The corresponding normalized distribution of LLEs for different realizations of the mean-field trajectories shows that larger m leads to sharper distributions. Numerically, we use interaction strength $J = 0.28$ for panels (a) and (b), and $J = 0.35$ for (c) and (d).

SM 4. EXPERIMENTAL REALIZATION

The kicked protocol discussed in the main text can be experimentally realized in superconducting quantum simulation platforms.

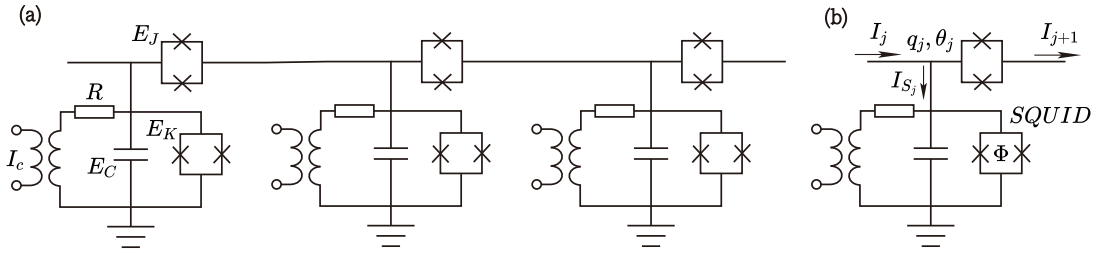


FIG. S5. (a) The experimental realization of our random kicked rotor model. Here we just show three of the rotors in the periodic boundary. (b) The circuit for the j^{th} kicked rotor.

We first consider the systems without dissipation and mutual inductance. As shown in Fig. S5(b), each rotor can be simulated by a resonator composed of one capacitor and superconducting quantum interference devices (SQUIDs). Each SQUID has two Josephson junctions to form a loop. The Hamiltonian of the resonator on the j^{th} site is $\hat{H}_j = \hat{q}_j^2/2C + E_K \cos(2\pi\Phi_K/\Phi_0) \cos(\hat{\theta}_j)$, where the first and the second term correspond to the capacitor and the SQUID, respectively. In the Hamiltonian, \hat{q}_j is the charge on the j^{th} capacitor, Φ_K is the total magnetic flux

of two Josephson junctions, $\Phi_0 = hc/(2e)$ is the Cooper-pair flux quantum, and $\hat{\theta}_j$ is their average phase. As shown in Fig. S5(a), by introducing one SQUID linking the j^{th} resonator with the $(j+1)^{\text{th}}$ resonator, $\hat{H}_{j,j+1} = E_J \cos(2\pi\Phi_J/\Phi_0) \cos(\hat{\theta}_j - \hat{\theta}_{j+1})$, one can now simulate the many-body interacting system. The phase Φ_J and Φ_K are tunable time-dependent parameters, which can control the strength of interaction and the on-site potential energy. Therefore, the Hamiltonian of the entire many-body system reads

$$\hat{H} = \sum_j \left\{ \frac{\hat{q}_j^2}{2C} + E_K \cos(\phi(t)) \cos(\hat{\theta}_j) + E_J \cos(\phi(t)) [\cos(\hat{\theta}_j - \hat{\theta}_{j+1}) + \cos(\hat{\theta}_j - \hat{\theta}_{j-1})] \right\},$$

where we set two magnetic fluxes the same, $\phi(t) = 2\pi\Phi_J(t)/\Phi_0 = 2\pi\Phi_K(t)/\Phi_0$. We can apply the driving pulses shown in Fig. S6, and if $T_1 \gg T_2$, $\cos(\phi(t))$ can approximately generate dynamical effects induced by periodic kicks $\delta(t)$ as considered in the main text.

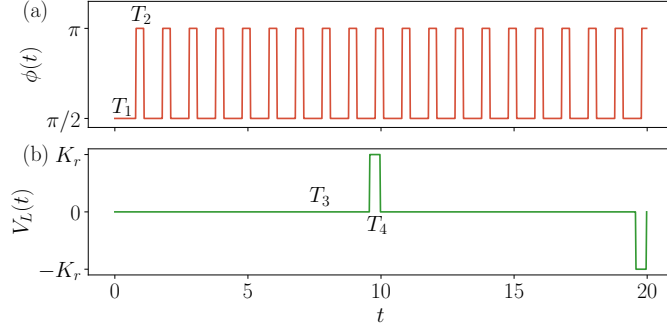


FIG. S6. Time-dependent protocol of $\phi(t)$ and $V_L(t) = MI_c(t)/R$ in the experimental setting to mimic the kicked rotor system. $\phi(t)$ generates periodic kicks and $V_L(t)$ generates random dipolar kicks to induce the time rouseau order.

Then we introduce dissipation and mutual inductance by connecting a branch composed of a resistor and an instrument transformer, as shown in Fig. S5(a). To simulate our model, we discuss EOMs under the classical approximation. In this approximation, we change $\hat{q}, \hat{\theta}$ to q, θ and obtain their equation of motion via the Poisson bracket. We denote the current moving from the $(j-1)^{\text{th}}$ resonator to the j^{th} resonator as I_j and the j^{th} resonator to the $(j+1)^{\text{th}}$ resonator as I_{j+1} shown in Fig. S5(b). These currents go through SQUIDs following the EOM,

$$\begin{aligned} I_j &= \frac{2e}{\hbar} E_J \cos(\phi) \sin(\theta_j - \theta_{j-1}), \\ I_{j+1} &= \frac{2e}{\hbar} E_J \cos(\phi) \sin(\theta_{j+1} - \theta_j). \end{aligned} \quad (\text{S.1})$$

We apply Kirchhoff's law and get $I_{S_j} = I_j - I_{j+1}$. Then the current splits into the capacitor with current \dot{q}_j , resistor with $(q_j/C - MI_c)/R$, and SQUIDs with $-\frac{2e}{\hbar} E_J \cos(\phi) \sin(\theta_j)$. One can also assume that the self-inductance of resonators is negligible. Then we get the EOM that mimics our kicked rotor model,

$$\dot{q}_j = -q_j/CR + \frac{2e}{\hbar} E_J \cos(\phi(t)) \sin(\theta_j) + \frac{2e}{\hbar} E_J \cos(\phi(t)) [\sin(\theta_j - \theta_{j-1}) + \sin(\theta_j - \theta_{j+1})] + MI_c(t)/R, \quad (\text{S.2})$$

where $I_c(t)$ denotes the control current that induces dipolar kicks. Its driving protocol is depicted in Fig. S6(b) and we also require $T_3 \gg T_4$ to approximate the delta kick. Note that the realization of the dipolar kicks can indeed be quite flexible in practice, for instance, the transformer can be replaced by any other voltage source.

By using the relation between the phase θ_j and voltage $U_j = q_j/C$, we obtain the other set of EOMs

$$\dot{\theta}_j = \frac{2eU_j}{\hbar} = \frac{2eq_j}{C\hbar}, \quad (\text{S.3})$$

where U_j is the voltage between two sides of SQUIDs and it is equal to the voltage of the capacitor. In conclusion, this circuit with EOMs Eqs. (S.2) and (S.3) can simulate our dipolar kicked many-rotor system.